

www.acsnano.org

Reversible Molecular and Ionic Storage Mechanisms in High-Performance Zn_{0.1}V₂O₅·nH₂O Xerogel Cathode for Aqueous **Zn-Ion Batteries**

Kaivue Zhu, Tao Wu,* Wessel van den Bergh, Morgan Stefik, and Kevin Huang*



Cite This: https://doi.org/10.1021/acsnano.1c03684



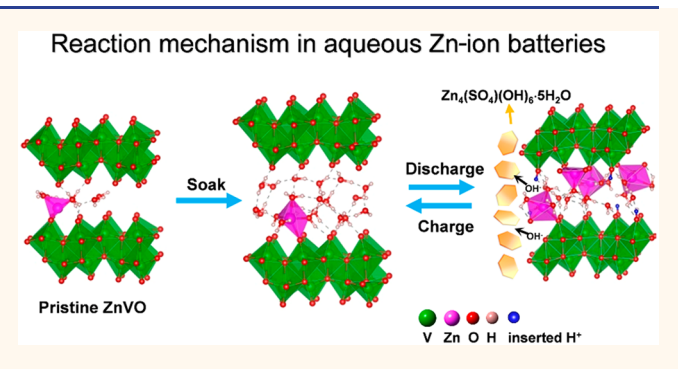
ACCESS

Metrics & More

Article Recommendations

Supporting Information

ABSTRACT: The cathode is a critical component for aqueous Zn-ion batteries (ZIBs) to achieve high capacity and long stability. In this work, we demonstrate a dissolution-free, low-Zn-preinserted bilayer-structured V2O5 xerogel cathode, Zn_{0.1}V₂O₅·nH₂O (ZnVO), with excellent capacity and stability using a low-cost ZnSO₄ electrolyte. Its discharge capacity reaches 463 mAh g⁻¹ at 0.2 A g⁻¹ and 240 mAh g⁻¹ at 10 A g⁻¹, while 93% and 88% of its capacity are retained at 0.2 A g⁻¹ for 200 cycles and at 10 A g⁻¹ for 20 000 cycles, respectively. We then show that the outstanding performance of ZnVO is derived from the enlarged gallery spacing by the solvent water intercalation and the water stable V2O5 bilayer structure. We



further unveil via ab initio molecular dynamics that H⁺ is largely originated from the dissociation of the gallery water, while OH moves out of the gallery to form Zn₄(SO₄)(OH)₆·5H₂O with ZnSO₄ electrolyte on the surface of ZnVO; the intercalated Zn^{2+} forms aquo complex $[Zn(H_2O)_6]^{2+}$ with the gallery water. Our theoretical analysis also suggests that the gallery water and solvent water in the electrolyte are statistically the same and functionally equivalent. Overall, this study shows the promise of ZnVO as a practical cathode for ZIBs and offers fundamental insights into the roles of gallery water, solvent water, bilayer V₂O₅ structure, and dual Zn²⁺/H⁺ intercalation mechanisms in achieving high capacity and long stability.

KEYWORDS: cathode, ab initio molecular dynamics, gallery water, bilayer V_2O_5 structure, hybrid H^+/Zn^{2+} intercalation

INTRODUCTION

The progress of aqueous Zn-ion battery (ZIB) technology toward commercialization relies critically upon solid fundamental understanding and materials advances to address the existing scientific and technical gaps such as capacity-durability trade-off and ambiguous H⁺/Zn²⁺ co-storage mechanisms.¹⁻ The capacity-durability trade-off, which refers to the highcapacity cycling at lower current densities often at a cost of stability, represents a major obstacle to ZIB technological advancement. The current understanding of this behavior is primarily based on the assumptions that (1) the high-degree ionic intercalation at low current densities weakens the structural integrity and (2) extended cation dissolution during the long cycle at low current densities results in loss of active materials. 8-10 For a layered cathode material with a large enough gallery spacing and adequate amount of structural water, the former mechanism is of less a concern, thus leaving the dissolution mechanism the primary cause for the capacity

decay. Therefore, developing dissolution-resistant cathodes for commercial ZIBs is of critical importance.

In recent years, V-oxides (e.g., α -V₂O₅, V₂O₅·nH₂O, H₂V₃O₈, VO2, etc.) have attracted much attention as ZIB cathodes, due to their layered (or tunnel) crystal structures and the multiple oxidation states of V (+3 to +5). 11-18 Among various V-based materials, anhydrous single-layer α -V₂O₅ was studied as a ZIB cathode; 12,19-21 however, it is slightly soluble in pure water, producing a characteristic pale yellow and acidic solution. 22-25 The current effort to mitigate the dissolution problem is to introduce larger cations (NH₄⁺, Li⁺, Na⁺, Ca²⁺, Zn²⁺, etc.) and

Received: April 30, 2021 Accepted: June 3, 2021



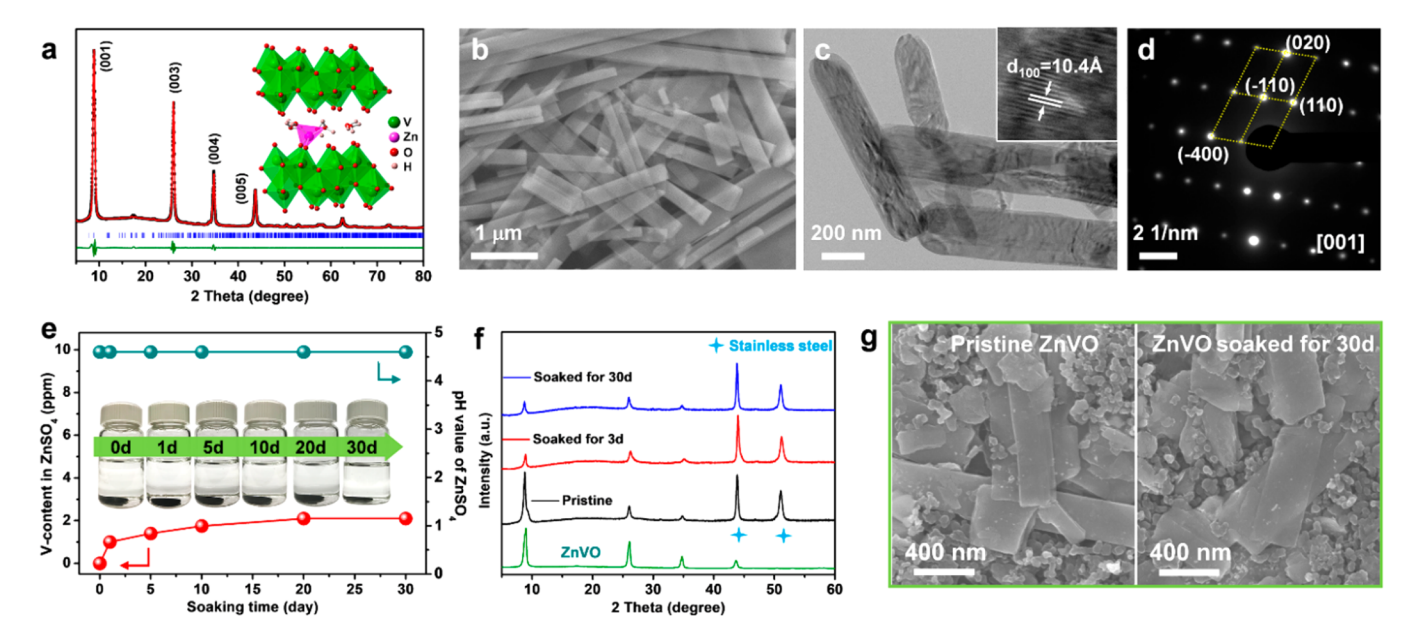


Figure 1. Structural and morphological characterization of ZnVO. (a) Experimental and Rietveld-refined XRD patterns with experimental data in black dots and the refinement in a red line; tick marks in blue and the curve in olive indicate the allowed Bragg reflections and difference between experiment and refinement, respectively. Inset: crystal structure of ZnVO viewed along the *b*-axis; (b) SEM image; (c) TEM image (inset: HRTEM image); (d) SAED pattern of ZnVO; (e) time-dependent V concentration (by ICP-OES) and pH in 2 M ZnSO₄ (10 mL) electrolyte after soaking with ZnVO (active mass: 2 mg). The insets are optical images of ZnVO/ZnSO₄ systems at different periods; (f) XRD patterns of dry ZnVO electrodes before and after soaking in 2 M ZnSO₄ electrolyte for 3 days and 30 days, respectively; (g) SEM images of ZnVO before (left) and after soaking in 2 M ZnSO₄ electrolyte for 30 days (right), respectively.

structural water into the base layered V_2O_5 structure, forming a so-called cation preinserted hydrated V_2O_5 xerogel; the additional ionic bonding provided by the secondary cations reduces the dissolution of the base material (e.g., V^{S+}). $^{26-32}$ While this strategy reduces the dissolution and improves the cycle stability, it also lowers the achievable capacity due to the lowered oxidation state of the V ion, hindered Zn-ion diffusion, and increased molecular weight of the active material.

In addition to the dissolution challenge, anhydrous α -V₂O₅ also has a small basal distance (~4.4 Å) as compared to hydrated Zn ions (~5.5 Å), which would strain the oxide lattice and make Zn-ion diffusion difficult during cycles.³³ In contrast, cation-inserted as well as bare V2O5·nH2O xerogels have a bilayer structure with a larger basal distance (11.5 Å for $n \sim 1.6$ and 8.7 Å for $n \sim 0.5$) and a beneficial "lubrication" effect, thus having been actively studied as a ZIB cathode. 11,34-37 While these bilayer V2O5 nH2O xerogel cathodes exhibit improved cycling stability over pure singlelayer anhydrous α -V₂O₅, the overall long-term cycle stability and level of capacity are still far from practicality. 20,28,36,38,39 One of the underlying reasons is their poor stability in highconcentration aqueous Zn-salt electrolytes such as ZnSO₄ and Zn(CF₃SO₃)₂. Although it is more preferable to use Zn-(CF₃SO₃)₂ than ZnSO₄ from a performance perspective, the cost of the former is ~28 times the latter. Therefore, developing stable, cation preinserted bilayer V₂O₅·nH₂O xerogel cathodes with low-cost ZnSO₄ electrolytes represents a viable path forward to solve the "capacity-stability-cost" trade-off for commercial ZIBs.

We herein report on a dissolution-free, stable, low-Zn-preinserted V_2O_5 xerogel ZIB cathode, $Zn_{0.1}V_2O_5$ · nH_2O (ZnVO), which is synthesized from a hydrothermal process with 1 M ZnSO $_4$ solution as the precursor. The rationale is that the product stable in the ZnSO $_4$ -containing hydrothermal

solution shall also be stable in $ZnSO_4$ solution in a ZIB cell. In this work, we investigate the stability of the obtained bilayer structured ZnVO in a 2 M $ZnSO_4$ and then test its capacity and stability in ZIB cells with a 2 M $ZnSO_4$ electrolyte. We show that ZnVO exhibits higher capacity and better stability than the previously reported $Zn_{0.25}V_2O_5\cdot nH_2O$ prepared in a diluted Zn^{2+} solution (0.026 M). Also different from this previous work, we focus on the fundamental understanding of how the bilayer V_2O_5 structure and gallery water in ZnVO, and solvent water in $ZnSO_4$ electrolyte, play an active role in achieving high capacity and stability through dual Zn^{2+}/H^+ storage mechanisms with convincing experimental and theoretical evidence.

RESULTS AND DISCUSSION

Characterization of Synthesized ZnVO. The $Zn_{0.1}V_2O_5$. nH₂O (ZnVO) was prepared through a controllable hydrothermal method by reacting 5 mM NH₄VO₃ with 1 M ZnSO₄ in an acidic solution with pH ~ 2.5 at 170 °C for 10 h, the details of which can be found in Section 1 of the Supporting Information (SI). The formation of pure ZnVO phase is confirmed by XRD and subsequent Rietveld refinement of Figure 1a. The inductively coupled plasma optical emission spectroscopy (ICP-OES) and thermogravimetric analysis (TGA) of Figure S1a informs us that the chemical stoichiometry of the as-prepared ZnVO is Zn_{0.1}V₂O₅·0.7H₂O. The Brunauer-Emmett-Teller (BET) surface area analysis in Figure S1b indicates the ZnVO with a specific surface area of 126 m² g⁻¹. The scanning electron microscope (SEM) and transmission electron microscope (TEM) images of Figure 1b,c reveal ZnVO with a nanobelts morphology. The crystal structure of ZnVO is also verified by high-resolution (HR) TEM and selected-area electron diffraction (SAED) shown in Figure 1c,d. The *d*-spacing is found to be 10.4 Å for the (100)

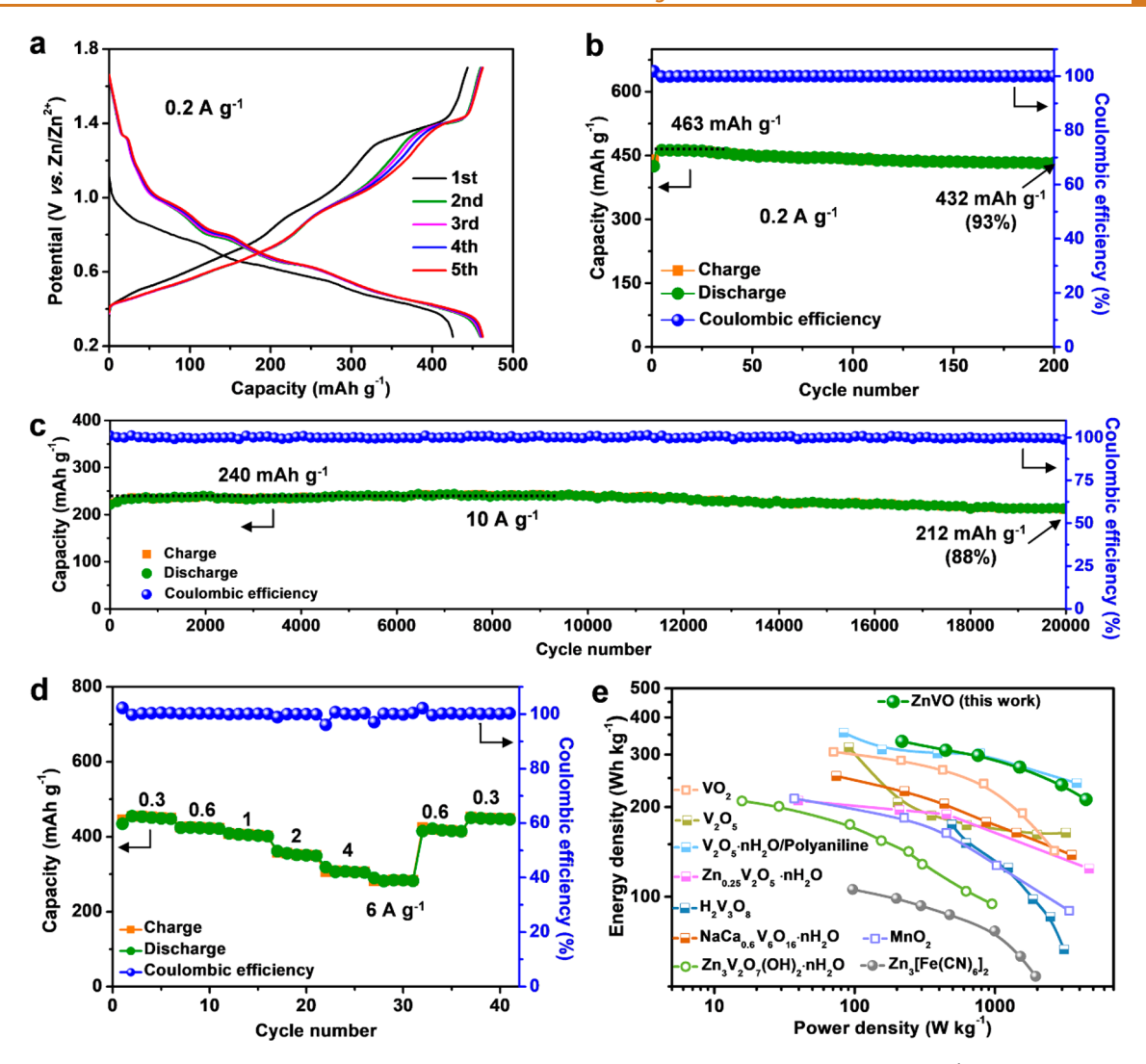


Figure 2. Electrochemical performance of ZnVO. (a) The initial five-cycle discharge/charge profiles at 0.2 A g^{-1} ; cycling performance at (b) low rate (0.2 A g⁻¹) and (c) high rate (10 A g⁻¹), respectively; (d) rate performance; (e) Ragone plot (energy density vs power densities) comparing ZnVO with other reported ZIB cathodes.

plane, which agrees with $d_{100}=10.42$ Å from the XRD refinement results. The SAED pattern in the inset of Figure 1d indicates the intrinsic single-crystal structure and is consistent with those refined crystallographic parameters of ZnVO. It is worth mentioning that, in the crystal structure of ZnVO (see the inset in Figure 1a), metal ion (Zn²⁺) and structural water are situated within galleries of V_2O_5 as "pillars" and "binder," respectively, to stabilize the layered structure.

The Ultra-stability of ZnVO in Low-Cost Aqueous ZnSO₄ Electrolytes. The most common anhydrous α -V₂O₅ suffers from severe dissolution in 2 M ZnSO₄ aqueous electrolyte, as shown in Figure S2a. In contrast, Figure 1e shows that the electrolyte solution after in contact with ZnVO remains colorless and the V concentration in the electrolyte (10 mL) stabilizes at 2 ppm, 30 times lower than 60 ppm for α -V₂O₅ even after a 30-day soak. The trace amount of V in the electrolyte is not surprising as even insoluble materials would reach equilibrium with water by dissolving a trace amount. If the dissolution reactions of ZnVO are like those of α -V₂O₅ (eq S1), the pH of ZnSO₄ solution would change from 4.6 to 4.4 (with 30 times less dissolution than α -V₂O₅). However, the pH of ZnSO₄ shown in Figure 1e stays at ~4.6 over the entire

soaking period, further confirming the high stability of ZnVO in ZnSO₄ electrolyte. In addition, Figure 1f shows XRD patterns of ZnVO vs soaking time, where intensities of the peaks at $\sim 26^{\circ}$ and $\sim 35^{\circ}$ are virtually unchanged, whereas the intensities at $\sim 8.5^{\circ}$ decrease considerably for the initial 3 days and then reach a steady state value for the subsequent 27 days. The decrease of peak intensity at $\sim 8.5^{\circ}$ at the beginning is due to the incorporation of solvent water into the gallery, which will be further discussed in detail in the following section. These results indicate the crystal structure of ZnVO is stable even after soaking for 30 days in 2 M ZnSO₄ electrolyte. Compared to the pristine ZnVO, the SEM image of Figure 1g also shows no morphology change, and the nanorod morphology is still well maintained after soaking for 30 days. Therefore, all the results confirm that ZnVO is stable in the ZnSO₄ electrolytes, which is a prerequisite for being a stable ZIB cathode.

Electrochemical Performance. The electrochemical performance of ZnVO as a cathode in ZIB is evaluated in a coin-cell type configuration consisting of a Zn-metal anode and aqueous 2 M ZnSO₄ electrolyte. Figure 2a shows the initial five-cycle galvanostatic discharge/charge profiles of ZnVO

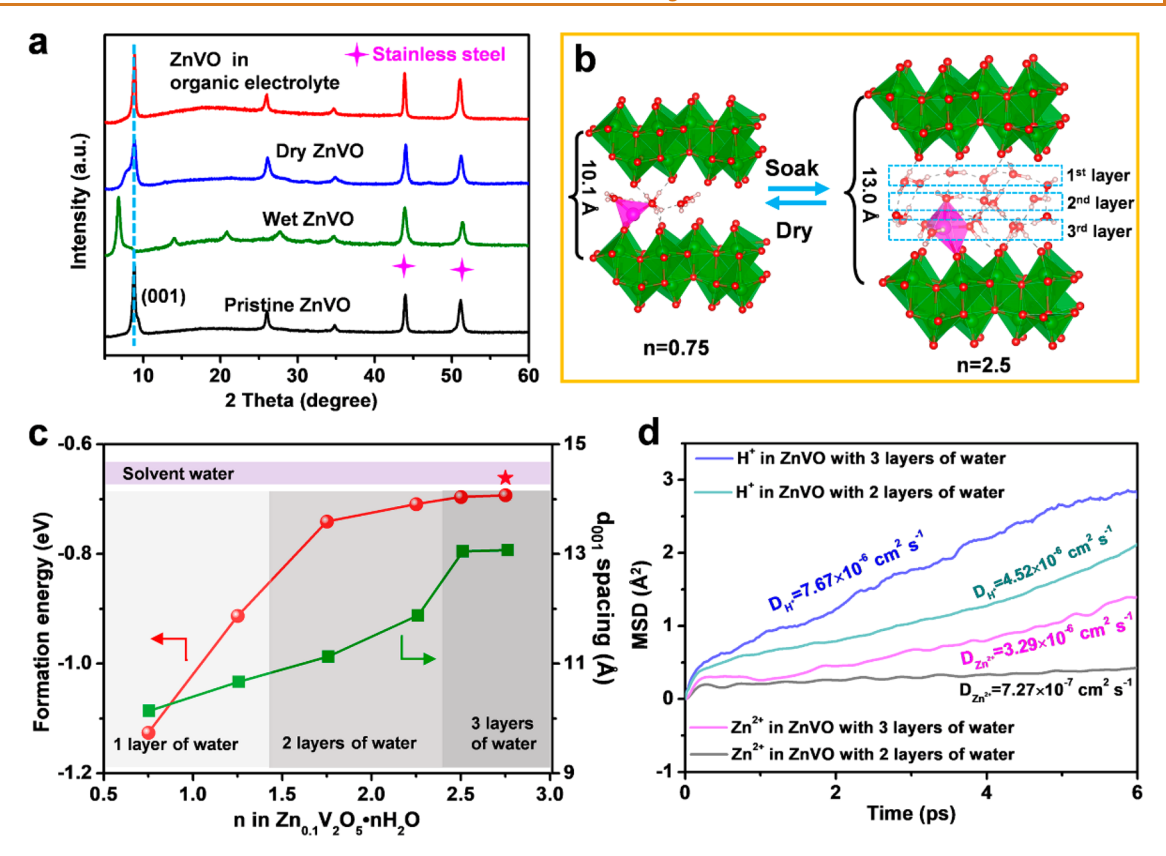


Figure 3. Intercalation of solvent water into ZnVO. (a) XRD patterns of ZnVO electrode at pristine state (Pristine ZnVO), soaked in 2 M ZnSO₄ electrolyte (Wet ZnVO), dried after soaking in ZnSO₄ electrolyte (Dry ZnVO), and soaked in 1 M Zn(CF₃SO₃)₂ organic solution (ZnVO in organic electrolyte); (b) a schematic illustration of the intercalation/extraction of solvent water in/from ZnVO's gallery after soaking/drying ZnVO in ZnSO₄ electrolyte; (c) average formation energy of water and d_{001} spacing in ZnVO with different gallery water contents. The red star represents the average formation energy of physiosorbed water without chemical bonding to the V₂O₅ bilayers. The purple area represents the formation energy range of solvent water; (d) total mean square displacement (MSD) of Zn²⁺ and H⁺ diffusion in bilayered V₂O₅ structures with 2 and 3 layers of water, respectively.

between 0.25 and 1.7 V vs Zn/Zn²⁺ at 0.2 A g⁻¹. ZnVO delivers an average capacity of 463 mAh g⁻¹ at 0.2 A g⁻¹. Figures 2b,c and S3 also show that the ZnVO cathode is reversible and durable at both low (0.2 A g⁻¹) and high (5 A g^{-1} , 10 A g^{-1}) rates. An impressive 93% of the highest capacity (463 mAh g^{-1}) is retained for 200 cycles at 0.2 A g^{-1} , and 88% for 20 000 cycles at 10.0 A g^{-1} . Even after 20 000 cycles at 10.0 A g-1, the morphology and crystal structure of ZnVO nanobelts are still well-maintained (see Figures S4 and S5). Compared to the performance of the previously reported $Zn_{0.25}V_2O_5$: $nH_2O_7^{31}$ i.e., capacity retention of 80% over 1000 cycles at 2.4 A g^{-1} , the performance of ZnVO in this study is evidently better. In addition, the ZnVO's performance is also better than or at least comparable to that of many recently reported high-performance ZIB cathodes such as VO_2^{-14} α -material; ⁴⁹ Table S1 provides a full comparsion. To further demonstrate the stability of ZnVO in ZnSO₄ electrolyte, Figure S6 shows a similar capacity and cycling performance between the pristine and ZnSO₄ pre-soaked (30 days) ZnVO electrodes. The excellent structural/chemical stability and electrochemical reversibility support the ultra-stability of ZnVO observed in Figure 2b-d. We acknowledge that Znanode corrosion/dendrite formation (see Figure S7) could

partially contribute to the instability,⁵⁰ but it is not the focus of this study.

The rate capability is further depicted in Figures 2d and S8; the discharge capacities are 450, 422, 408, 362, 317, and 280 mAh g⁻¹ at 0.3, 0.6, 1.0, 2.0, 4.0, and 6.0 A g⁻¹, respectively. ZnVO shows good recovery of capacity upon returning to lower current densities. The insensitivity to the current density infers that ZnVO has good structural flexibility and stability against guest species intercalations. The fundamental reason for the high-rate capability lies in the large gallery spacing widened by solvent water as well as the pseudocapacitive effect, which is discussed in Section 1 of the SI (Figures S9–S11). Benefiting from the large gallery spacing and the involvement of solvent water, the ZnVO cathode shows much higher pseudocapacitive contribution than other V-based materials, such as NaV₃O₈·1.5H₂O, V₅O₁₂·6H₂O, and Li₃V₂(PO₄)₃.⁵¹⁻⁵³ Because of its excellent rate capability, Figure 2e of the Ragone plot (energy density vs power density) indicates that ZnVO is among the best cathodes for ZIBs. 13,14,21,31,40-45 To be specific, the ZnVO-based ZIB exhibits an energy density/ power density of 332 Wh kg⁻¹/217 W kg⁻¹ and 212 Wh kg⁻¹/ 4445 W kg⁻¹ (based on the mass of ZnVO) at 0.1 and 6.0 A g⁻¹, respectively. Apart from the aqueous safety, the excellent rate capability and cycling stability ensure the battery to be charged/discharged at a fast rate with a long cycle life, which is desirable for large-scale stationary energy storage.

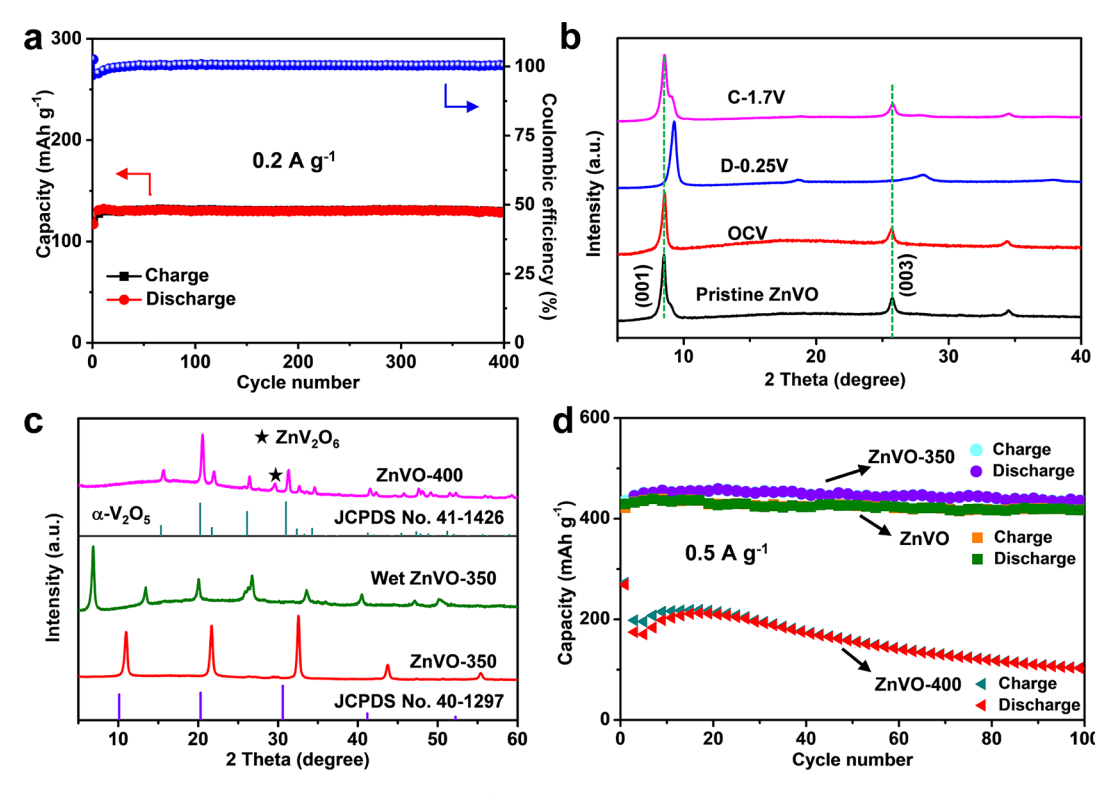


Figure 4. Role of solvent water and bilayer structured V_2O_5 . (a) Cycling performance of ZnVO in 1 M Zn(CF₃SO₃)₂-acetonitrile electrolyte at 0.2 A g⁻¹; (b) ex situ XRD patterns of ZnVO cathode after cycled in 1 M Zn(CF₃SO₃)₂-acetonitrile electrolyte; (c) XRD patterns of ZnVO powders calcinated at 350 and 400 °C, respectively; (d) cycling performances of ZnVO, ZnVO-350, and ZnVO-400, respectively, at 0.5 A g⁻¹ with a 2 M ZnSO₄ aqueous electrolyte.

We also provide a broad phasal, microstructural, and spectroscopic evidence in sections 2 and 3 of the SI to support the dual $\rm H^+/Zn^{2^+}$ intercalation/deintercalation into/from ZnVO, which is a well-accepted storage mechanism for ZIBs, through state-of-charge (SOC) dependent compositions (see Figures S12–S15) and phase evolution (see Figures S16, S17) studies. From a theoretical perspective, the density functional theory (DFT)-calculated Gibbs free energies of formation of Zn^{2^+} and H^+ in ZnVO are -2.94 and -0.86 eV, respectively, with the initial H^+ and Zn^{2^+} intercalated structure shown in Figure S18. The negative formation energies suggest that both Zn^{2^+} and H^+ intercalations into ZnVO are thermodynamically favorable.

Critical Roles of Gallery Water and Bilayer Structure of ZnVO Xerogel Cathode. It is interesting to observe gallery expansion of ZnVO after soaking in 2 M ZnSO₄. Figure 3a of XRD patterns shows that the (001) peak of ZnVO is shifted to lower 2θ with the corresponding d_{001} increasing from 10.1 to 13.0 Å after soaking for 2 h. After drying, the XRD pattern of the sample becomes the same as that of the pristine one (before soaking). This finding suggests that the solvent water in the electrolyte solution can reversibly move in and out of the ZnVO's gallery. Note that no observation of a left shift of the (001) peak of ZnVO in Figure 3a after soaking in 2 M ZnSO₄ electrolyte for 3 days is due to the fact that ZnVO was dried before performing XRD. In contrast, the XRD pattern for ZnVO soaked in organic 1 M Zn(CF₃SO₃)₂ electrolyte (1 M Zn(CF₃SO₃)₂ in acetonitrile) remains unchanged, suggesting that no molecules are inserted into the ZnVO's gallery. In addition, Figure S19 shows that the (001) peak of ZnVO is also shifted to lower 2θ after soaking in a pure deionized (DI) water, further suggesting that it is the water incorporation that

causes gallery expansion. Therefore, it is concluded that the solvent water can be intercalated into the gallery of ZnVO upon immersion into the ZnSO $_4$ solution. According to previous reports, the 2.9 Å increase in the gallery spacing corresponds to an intercalation of two additional layers of water. 31,34

To understand the water intercalation behavior and explore its fundamental driving force, we performed DFT calculations on how the d_{001} spacing changes with the amount of water in the gallery of ZnVO. On the basis of the chemical stoichiometry of the as-prepared ZnVO ($Zn_{0.1}V_2O_5 \cdot 0.7H_2O$), we constructed the model with a similar chemical stoichiometry (Zn_{0.1}V₂O₅·0.75H₂O) for convenience. The DFToptimized d_{001} spacing is 10.14 Å with one-layer water in the gallery (see Figure 3b), which matches well with the measured d_{001} spacing (10.1 Å). As water is gradually added into the gallery, the calculated d_{001} spacing increases, reaching 13.0 Å after adding two more layers of water (see Figure 3b,c, green line), which also agrees well with the experimental values of 13.0 Å of ZnVO after soaking in 2 M ZnSO₄. The corresponding crystal structures of ZnVO constructed at various H₂O contents in the gallery are illustrated in Figure S15. With the perfect d_{001} matching between the theoretical and experimental values, we are confident in that the following energetics calculations of water formation and ab initio molecular dynamics (AIMD) simulations based on these structural models will be reliable.

It is worth mentioning that, among the three layers of water in the ZnVO's gallery after water intercalation (see Figure 3b), the 1st and 3rd water layers are bonded with the V-O bilayers through H-bonding, whereas the middle 2nd layer water does not bond to the V-O layer. Thus, the 1st and 3rd water layers

are expected to exhibit a lower formation energy than that of the 2nd layer water. Figure 3c shows the calculated average water formation energy in the ZnVO's gallery vs H2O content in the gallery. Starting from the ZnVO with one layer of water $(d_{001} = 10.1 \text{ Å})$, we find the average water formation energy increases with water intercalation, suggesting that the water intercalation process will become more and more difficult with increasing water content in the gallery. The average water formation energy finally converges to -0.70 eV with all three layers of water in the gallery and a d-spacing of 13.0 Å. At this configuration, the formation energy of the gallery water in ZnVO is at probability equilibrium with that of solvent water in the electrolyte; i.e., the formation energy of the gallery water in ZnVO is statistically indifferent from solvent water in the electrolyte. In other words, the structural water in the gallery can be virtually treated the same as solvent water in the electrolyte. To verify this hypothesis, we calculated the formation energy of solvent water with different space groups: Cmc21, P63cm, and P1. The calculated values range from -0.67 to -0.64 eV, which is represented by the purple region in Figure 3c. Note that the calculated average 3-layer water formation energy of ZnVO is -0.70 eV, which is slightly lower than that of solvent water. However, as we emphasized before, the waters bonded with the V₂O₅ bilayers, i.e., 1st and 3rd layer water in Figure 3b, have a formation energy lower than -0.70eV, which implies that solvent water will bond to the V₂O₅ bilayers during the soaking process before the 2nd layer water intercalation into the middle. The 2nd water layer has a formation energy of -0.66 eV, which is very close to $-0.67 \sim$ -0.64 eV of formation energy of the solvent water. Therefore, the driving force of water intercalation into the ZnVO gallery is the difference in formation energy between the gallery and solvent water.

With the presence of gallery water, our DFT calculations further reveal enhanced Zn-ion diffusion. Shown in Figure 3d is the AIMD-calculated total mean square displacement (MSD) of Zn²+ diffusion in the bilayered V_2O_5 structure with 2 and 3 layers of water, respectively; the Zn^{2+} diffusion coefficient with 3 layers of water is 3.29 \times 10 $^{-6}$ cm² s $^{-1}$, which is almost 5 times larger than that with 2 layers of water (7.27 \times 10 $^{-7}$ cm² s $^{-1}$). The enhanced Zn²+ diffusion is mainly resulted from the enlarged gallery spacing by the water intercalation.

To further verify the above fundamental understanding of the water effect, we have also performed a cycling experiment using a nonaqueous electrolyte (1 M Zn(CF₃SO₃)₂ in acetonitrile). Figures 4a and S21 show a low capacity of 130 mAh g⁻¹ at 0.2 A g⁻¹. The much lower capacity than aqueous electrolytes directly supports the promotional role of solvent water and indirectly supports that H⁺ intercalation indeed occurs in ZnVO and contributes to a significant portion of the overall energy storage capacity. Figure 4b of ex situ XRD patterns of ZnVO cathode at different SOCs with a nonaqueous electrolyte indicates that the (001) peak is gradually shifted toward a higher 2θ position during discharge, inferring a gradual contraction of the gallery spacing by the Zn²⁺-V₂O₅ attraction. On the other hand, there is no Zn₄(SO₄)(OH)₆·5H₂O (ZSH) found on the surface of ZnVO, implying no H⁺ intercalation. During the charge from 0.25 to 1.7 V, a reverse change in (001) spacing is observed, indicating Zn²⁺ extraction from the gallery. This observation is the same as that observed in aqueous electrolytes except that there is no involvement of water, H⁺ intercalation, and ZSH formation in nonaqueous electrolytes.

The XRD patterns of Figure 4c and TGA of Figure S22 show that the structural water in ZnVO can be removed by firing ZnVO at 350° in air without destroying the bilayer structure. The XRD pattern of ZnVO-350 is like that of standard V₂O₅·0.5H₂O (JCPDS No. 41-1426), but with a higher 2θ , inferring that the ZnVO-350 possesses a bilayer V₂O₅ structure with a smaller gallery spacing in the absence of gallery water. However, XRD patterns of wet ZnVO-350 are the same as those of the as-synthesized ZnVO after soaking in ZnSO₄ aqueous electrolyte. This means that the solvent water in ZnSO₄ aqueous electrolyte can enter the gallery of V₂O₅ bilayers no matter whether there are pre-existing gallery waters or not. That is, after soaking in aqueous electrolyte, solvent water enters the interlayers of V₂O₅ bilayer structures for both ZnVO and ZnVO-350 and the final materials are the same (see the XRD patterns in Figures 3a and 4c). Therefore, ZnVO and ZnVO-350 show similar cycling performance. The slight difference in capacities of ZnVO and ZnVO-350 is due to the normalized capacity to the mass of the initial materials of ZnVO and ZnVO-350, rather than the mass of final materials after soaking, which is difficult to determine. Therefore, it is the V₂O₅ bilayer structure rather than the pre-intercalated gallery waters that governs the ability of solvent waters to enter/exit the gallery and expand/contract its d-spacing.

However, the bilayer V₂O₅ structure will be destroyed above 400 °C. Figures 4c and S23 show that ZnVO-400 consists of mainly single-layer α -V₂O₅ and minor ZnV₂O₆. Because of the serious dissolution in ZnSO₄ aqueous electrolyte and much smaller interlayer spacing (\sim 4.4 Å) of α -V₂O₅ (see Figure S2), the ZnVO-400 shows much lower capacity and poorer cycling performance than ZnVO and ZnVO-350. The excellent cycling performance of ZnVO and ZnVO-350 indicates the criticality of V₂O₅ bilayers in rendering solvent water to shuttle freely between V₂O₅ bilayers and electrolyte. The enlarged gallery spacing by solvent water from the electrolyte is one of the reasons for the good capacity and cycle durability observed. It should be mentioned that the slightly higher capacity of ZnVO-350 ($Zn_{0.1}V_2O_5$) than as-prepared ZnVO ($Zn_{0.1}V_2O_5$) 0.7H₂O) shown in Figure 4d is likely attributed to the higher theoretical capacity of the former, i.e., 539.6 vs 505.8 mAh g⁻¹, given the fact that they have the same crystal structure but different molecular weight.

To further demonstrate the advantage of the V₂O₅ bilayer over single-layer α-V₂O₅, a pure hydrated bilayered V₂O₅ (H-V₂O₅) was prepared for dissolution study in ZnSO₄ electrolyte. Figure S24a-c shows that the pH value of ZnSO₄ is constant at 4.6 over the entire soaking period; meanwhile, the electrolyte solution remains colorless and the V concentration in the electrolyte (10 mL) stabilizes at 5 ppm, also much lower than 60 ppm for α -V₂O₅, after 30-day soaking. The dissolved V is slightly higher than 2 ppm of ZnVO, suggesting that ZnVO is more stable than H-V₂O₅ in ZnSO₄. The XRD patterns and SEM images of H-V₂O₅ vs soaking time are shown in Figure S24d-f, which show no phase transformation and no morphology changes after 30-day soaking. Again, the bilayer V₂O₅ structure is a key factor to achieve stable performance for a ZIB cathode. Although the V dissolution in ZnSO₄ is marginal for both ZnVO and H-V₂O₅, Figure S25 clearly shows ZnVO exhibits more stable cycling performance than $H-V_2O_5$, implying that the preinserted Zn²⁺ in ZnVO also helps the cycle stability. Therefore, water (gallery or solvent water), the bilayer V₂O₅ structure, and preinsertion of Zn²⁺ are the three

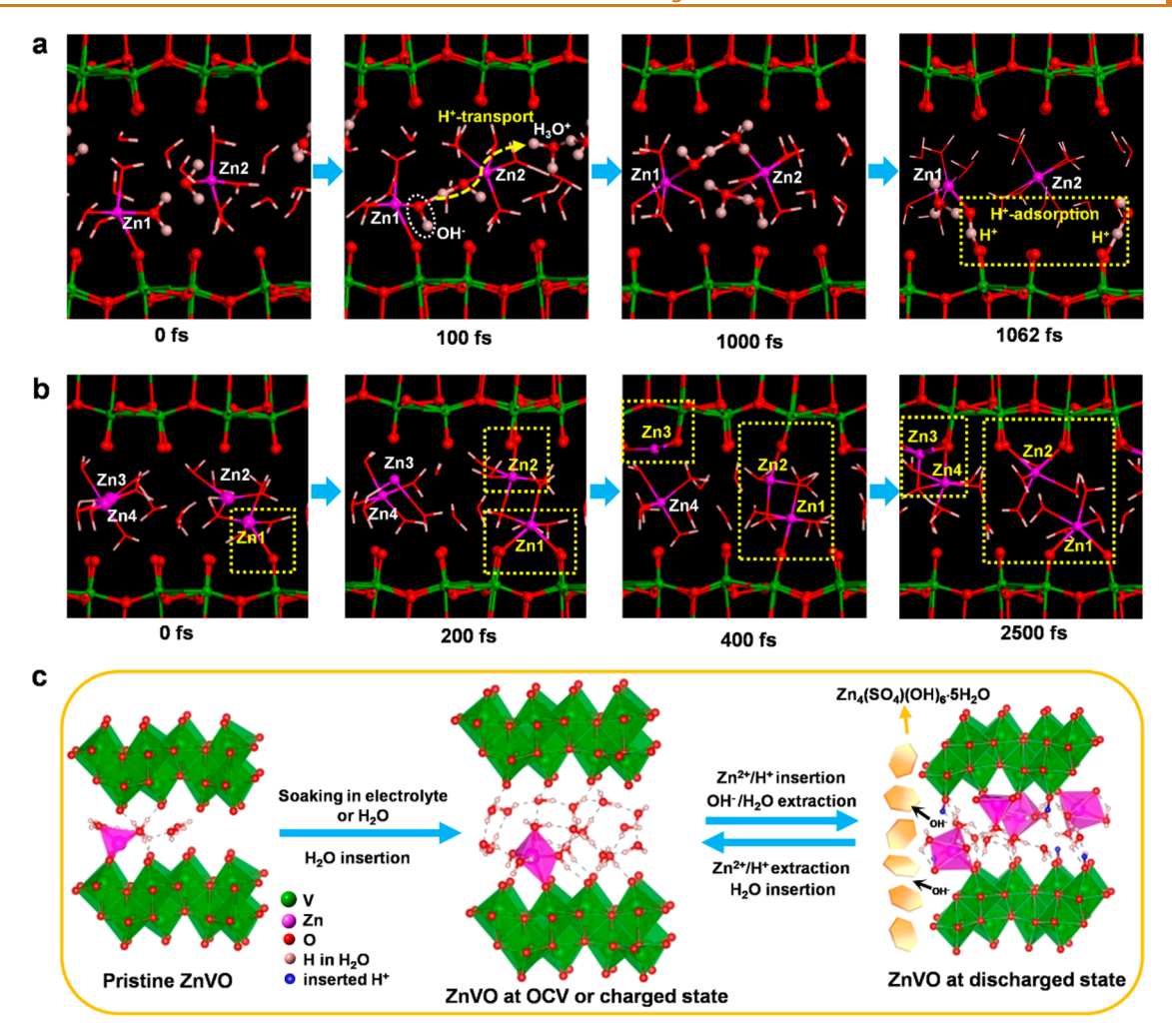


Figure 5. Reaction mechanisms of ZnVO in ZIBs. Snapshots of typical surface redox processes for (a) H^+ and (b) Zn^{2+} ; the magenta, green, red, and pink balls represent Zn, V, O, and H, respectively; (c) a schematic illustration of reaction mechanisms of ZnVO with the dissociation of gallery water and Zn^{2+}/H^+ .

critical elements for ZnVO to achieve high cycle stability in ZIBs.

Storage Mechanisms from AIMD. To understand the dual Zn²⁺/H⁺ intercalation mechanisms at the atomic scale, we performed AIMD simulations at 300 K. Figure 5a,b shows few representative snapshots of transport, adsorption, and surface redox processes for Zn²⁺ and H⁺ within the gallery of ZnVO. In Figure 5a, the simulation model contains three layers of water and two Zn²⁺ with a gallery spacing of 13.0 Å, which represents the situation of the very beginning stage of a discharge. At the initial state, one Zn²⁺ is bonded with O in the V₂O₅ bilayer, and the other one is surrounded by water molecules in the middle of the gallery. As the time elapses, we observe H⁺ undergoing three sequential processes: (1) water dissociation into H⁺ and OH⁻ (see the 2nd snapshot), (2) H⁺ transport (see the 2nd snapshot), (3) H⁺ surface adsorption (see the 4th snapshot), and (4) H+ redox reaction (charge transfer) (see the 4th snapshot). This result suggests that the origin of H+, a contributor to the overall capacity, is the gallery water. Meanwhile, OH⁻ from the water dissociation moves out of the gallery and reacts with ZnSO₄ electrolyte at the surface of ZnVO to precipitate out ZSH nanoflakes. This also explains why there are neither precipitates nor obvious pH changes inside the aqueous ZnSO₄ electrolyte during cycling. The consumption of gallery water by the dissociation is, therefore,

another reason, in addition to the Zn²⁺-O²⁻ interaction, for the shrinkage of gallery spacing during discharge, since the gallery spacing decreases appreciably with decreasing the number of gallery water. We also examined whether solvent water in the electrolyte can be another source of H⁺. Figure S26 shows two H⁺ (presumably from solvent water) and two Zn²⁺ in the gallery of ZnVO. Within 10 ps, AIMD simulations suggest that H⁺ transport and surface redox reactions are virtually the same as those for the gallery water shown in Figure 5a, which further supports the early conclusion that gallery and solvent waters behave virtually the same as the source of H+ stored in the ZnVO gallery during discharge. Another interesting observation from AIMD simulations is that the Zn²⁺ initially bonded with O2- will gradually migrate toward the middle of the gallery, forming an aquo Zn^{2+} complex ($[Zn(H_2O)_6]^{2+}$) with the gallery waters nearby (see the 3rd and 4th snapshots in Figure 5a). In other words, Zn²⁺ is in the form of hydrated Zn²⁺ at the initial discharge state when the gallery spacing is

As more Zn^{2+} are intercalated into the ZnVO gallery, the gallery spacing will shrink because of Zn^{2+} - O^{2-} interaction and consumption of gallery water as mentioned above. To simulate the dynamic state of Zn^{2+} in the gallery at this stage, we constructed a model containing four Zn^{2+} and two layers of water (some water has been presumably consumed at this

point of discharge) with a gallery spacing of 11.80 Å, for AIMD simulations. Figure 5b shows that, at the beginning (0 ps), only one Zn1 ion is bonded to the V-O layer. The other Zn2 is in the middle of the gallery as $[Zn(H_2O)_6]^{2^+}$. As the time elapses, Zn2, Zn3, and Zn4 ions are shown to successively enter the gallery and bond to the V-O layer in the following snapshots, resulting in a gradually shrinking gallery. Meanwhile, Figure S27 indicates that H⁺ from the gallery water dissociation can also bond to the V-O layer, contributing to capacity. These results suggest that the Zn²⁺ charge transfer process takes place in a shrinking gallery, accompanied by gallery water dissociation in the form of H⁺ and OH⁻.

On the basis of the above results, we here propose the dual Zn^{2+}/H^+ storage mechanisms in ZnVO with a bilayer structure as follows:

• At the OCV state, the solvent water in the electrolyte intercalates into ZnVO galleries to its saturation, becoming the gallery water and enlarging the gallery.

$$Zn_{0.1}V_2O_5 \cdot 0.7H_2O + 1.8H_2O \rightleftharpoons Zn_{0.1}V_2O_5 \cdot 2.5H_2O$$
(1)

 At the very beginning of the discharge stage, the gallery water is dissociated into H⁺ and OH⁻ according to the Brønsted-Lowry theory

$$H_2O_{(acid)} + H_2O_{(base)} \rightleftharpoons H_3O^+ + OH^-$$
 (2)

by which H^+ (H_3O^+) is further bonded to the V-O layer, while OH^- is expelled out of the gallery and react with Zn aquo complex $[Zn(OH)]^+$ and $SO_4^{\,2-}$ in the electrolyte to form ZSH:

$$4[Zn(OH)]^{+} + 5H_{2}O + SO_{4}^{2-} + 2OH^{-}$$

$$\Rightarrow Zn_{4}(SO_{4})(OH)_{6} \cdot SH_{2}O(ZSH) \downarrow$$
(3)

The Zn aquo complex [Zn(OH)]⁺ is prevalent in mildly acidic ZnSO₄ solutions according to the Brønsted–Lowry equilibrium:

$$[Zn(H_2O)_6]^{2+} + H_2O \rightleftharpoons [Zn(OH)(H_2O)_5]^+ + H_3O^+$$
(4)

$$[Zn(OH)(H_2O)_5]^+ \rightleftharpoons [Zn(OH)]^+ + 5H_2O$$
 (5)

Note that the Zn²⁺/V-O layer interaction and gallery water consumption are the two primary reasons for the gallery contraction during discharge.

- At a later stage of the discharge, more Zn²⁺ enter the gallery, forming [Zn(OH)₆]²⁺ aquo complex with the gallery water, with which both Zn²⁺ and H⁺ bond to the V-O layer and contribute to capacity.
- The above processes are reversed during the charge cycle.
- Throughout the cycle, ZnVO does not experience any phase/structure transformation; the only change is its gallery spacing to accommodate Zn²⁺, H⁺, and H₂O.

Figure 5c schematically illustrates the proposed multi-ion/molecule intercalation/extraction process occurring in bilayer structured ZnVO during a typical cycle. We acknowledge that it is difficult to determine the actual contents of H^+ and Zn^{2+} in the discharged ZnVO due to the lack of reliable techniques. NMR has been previously used to detect H; however, H in the gallery H_2O and crystal H_2O in ZSH interferes with the quantification of H concentration in ZnVO.

CONCLUSION

In this study, we have successfully synthesized a dissolutionfree and ultra-stable Zn-preinserted V2O5-bilayer xerogel cathode, Zn_{0.1}V₂O₅·0.7H₂O (ZnVO), for low-cost ZnSO₄ aqueous electrolyte based ZIBs. The crystal structure and morphology of ZnVO are well-maintained even after soaking in ZnSO₄ aqueous electrolyte for 30 days, indicating ZnVO's high compatibility with aqueous electrolytes. The ZIB cell's capacity reaches $463~\text{mAh}~\text{g}^{-1}$ at $0.2~\text{A}~\text{g}^{-1}$ and remains at 240~mmAh g^{-1} at 10 A g^{-1} , while 93% and 88% of its capacity are retained at 0.2 A g^{-1} for 200 cycles and at 10 A g^{-1} for 20 000 cycles, respectively. Throughout cycles, the ZnVO gallery undergoes a reversible contraction and expansion without changing the structure, nor forming other phases. Water as a gallery enlarger and H⁺ source and the dissolution-free bilayer V₂O₅ structure have been identified as two critical factors for the observed high capacity and excellent stability. AIMD simulations unravel that the origin of H⁺ as a major capacity contributor resulted from the dissociation of gallery water during discharge and the latter is equivalent to solvent water in the electrolyte. Another discharge product of the water dissociation, OH-, will move out of the gallery and react with the aquo Zn^{2+} complex and SO_4^{2-} in the electrolyte at the interface to form ZSH nanoflakes precipitates. The interactions between Zn ion and V2O5 bilayer and the consumption of gallery water are the two major reasons for the gallery contraction during discharge. Overall, the fundamental insights gained from this study have deepened our understanding of aqueous ZIB chemistry and lay the foundation for future discovery of better ZIB cathodes and the development of viable strategies to improve the ZIB performance.

EXPERIMENTAL METHODS

Synthesis of $Zn_{0.1}V_2O_5\cdot nH_2O$ (ZnVO) Xerogel. The ZnVO xerogel is prepared through a hydrothermal method. In a typical procedure, 0.5 mmol of ammonium metavanadate (NH $_4$ VO $_3$) was dissolved in 40 mL of deionized (DI) water under vigorous stirring at 90 °C for 2 h. Meanwhile, 100 mmol of zinc sulfate (ZnSO $_4$) and 5 mmol of sodium dodecyl sulfate (SDS) were dispersed in 60 mL of deionized water. The two solutions were then mixed, followed by adjusting the pH value by adding 1 M sulfuric acid to about 2.5. After stirring at room temperature for 20 h, the red solution was loaded into a 200 mL autoclave with a Teflon liner and held at 170 °C for 10 h. After the reaction, the dark-green precipitate is collected and thoroughly washed with deionized water and ethanol and finally dried at 60 °C for 12 h.

Materials Characterization. Phase and Structure Determination. Ex situ X-ray diffraction (XRD) patterns of the samples were collected using a Rigaku D/MAX-2100 with Cu Kα radiation (λ = 1.5418 Å). The data were recorded from 5° to 80° with an interval of 0.02° and a scan speed of 2° min⁻¹. In situ transmission XRD was also conducted using a SAXSLab Ganesha. A Xenocs GeniX 3D microfocus source was used with a copper target to produce a monochromatic beam with a 0.154 nm wavelength. The wide-angle X-ray scattering (WAXS) data were acquired with an X-ray flux of ~36.3 M photon per second incident upon the sample and a sample-to-detector distance of 90 mm under atmospheric conditions due to the use of aqueous electrolyte. A BioLogic SP-150 was employed for electrochemical measurements during in situ battery cycling at a current density of 0.2 A g⁻¹, while WAXS data were acquired continuously during in situ cycling with a 10 min exposure per frame.

Microstructure. The morphologies of the samples were captured with a Zeiss Ultra plus field emission scanning electron microscope (FESEM). The crystal structures and morphologies of samples were also acquired with a high-resolution transmission electron microscope (HRTEM, H9500) operated at 300 kV. Elemental mapping along

with morphology were obtained by a scanning transmission electron microscope (STEM, HD2000) equipped with an energy-dispersive X-ray spectrometer (EDS).

Thermal Analysis. Thermogravimetric analysis (TGA) was performed using a Netzsch STA 448 TGA (Germany) thermal analyzer. Specimens were placed in an Al_2O_3 crucible with a lid, and TGA data were recorded under air with a flow rate of 50 mL min⁻¹ while ramping from room temperature to 600 °C at a rate of 2 °C min⁻¹, and then cooling naturally to room temperature.

Chemical Analysis. The concentrations of elements of interest were analyzed by an inductively coupled plasma optical emission spectrometer (Shimadzu Corporation ICPS-8100).

Surface Chemistry. The surface chemical compositions and oxidation states of the cations were analyzed by X-ray photoelectron spectroscopy (XPS, Kratos AXIS 165, Clemson University) with Al Ka X-ray radiation ($h_{\lambda}=1486.6$ eV). Prior to these analyses, the cycled electrode powders were washed thoroughly with DI water to remove any electrolyte residue and then dried in a glovebox. All the binding energies were corrected by adventitious C 1s at 284.6 eV.

Electrochemical Characterization. Battery Cell Assembly. Electrochemical tests were carried out on CR2032-type coin cells. To prepare a ZnVO electrode, 60 wt % ZnVO xerogel, 26 wt % Super-P, and 14 wt % polyvinylidene fluoride (PVDF) were thoroughly mixed and dispersed into N-methyl pyrrolidone (NMP). The resultant slurry was then coated uniformly onto a 14 mm diameter stainless steel mesh, resulting in an ~1.2 mg cm $^{-2}$ active mass loading, followed by vacuum drying at 90 °C for ~12 h and compression at 10 MPa. In a full ZIB cell, zinc foil was used as the anode, 2 M ZnSO₄ as the electrolyte, and glass microfiber filters (Whatman, Grade GF/A) as the separator.

Electrochemical Testing. The CR2032-type coin cells were assembled in air and tested using a LAND battery testing system (CT2001A) within a potential window of $0.25-1.70~\rm V~(vs~\rm Zn/Zn^{2+})$. Cyclic voltammograms (CV) and electrochemical impedance spectroscopy (EIS) were performed in a three-electrode configuration using a Solartron 1260/1287 electrochemical workstation. A Zn ring and Zn plate were used as reference and counter electrodes, respectively. The EIS measurements were carried out at open circuit voltage (OCV) with an AC amplitude of 10 mV in a frequency range of 100 kHz and 0.1 Hz. The galvanostatic intermittent titration technique (GITT) was used to determine ionic diffusivity from a series of galvanostatic discharge pulses of 10 min at 50 mA g⁻¹, followed by a 1 h relaxation. The total ionic diffusion coefficient ($D_{\rm ion}^{\rm GITT}$) is calculated by ⁵⁴

$$D_{\rm ion}^{\rm GITT} = \frac{4L^2}{\pi\tau} \left(\frac{\Delta E_{\rm s}}{\Delta E_{\rm t}}\right)^2 \tag{6}$$

where τ is the constant current pulse time; L corresponds to the ion diffusion length, which equals the thickness of the electrode; $\Delta E_{\rm s}$ is the change of steady-state voltage during a single-step GITT experiment, and ΔE_t is the change in cell voltage at a constant current minus IR-loss during each galvanic step.

DFT Calculations. Geometric optimizations were performed based on the Kohn–Sham formalism of density functional theory (DFT) using the Vienna *Ab initio* Simulation Package (VASP) with the Perdew–Burke–Ernzerhof (PBE) exchange-correlation functional. $^{55-57}$ The projector augmented wave (PAW) method was applied to describe the interaction between electrons and ions. 58,59 To account for strong on-site Coulombic interactions of the V 3d electrons, we employed the DFT+*U* formalism with U = 3.25 eV. The Grimme's DFT+D3 method was used to account for van der Waals interactions between H₂O and V-O layers. The lattice constants and atomic positions were optimized with a cutoff energy of 400 eV for the plane-wave basis. The total energies and Hellmann–Feynman forces acting on atoms were converged below 10^{-5} eV per atom and smaller than 0.05 eV Å⁻¹, respectively. The Brillouin zone was sampled using a Γ-centered grid with a 2 × 4 × 2 *k*-point mesh.

To model V_2O_5 : nH_2O , we create the crystal structure of bilayer V_2O_5 without H_2O , and then adding H_2O molecules stepwise into the

gallery spacing, followed by the full optimization. The model was finalized based on agreement with the experimentally obtained gallery spacing of V_2O_5 : nH_2O . After an optimized gallery spacing was obtained, ab initio molecular dynamics (AIMD) simulations were performed in canonical ensemble (NVT) with a Nose thermostat at 300 K for 10 ps (with a time step of 1 fs). $^{62-64}$ The simulated system is considered well equilibrated when the temperature is stabilized, which is usually achieved after a few picoseconds. From the time-dependent trajectory, we can obtain ions' time-dependent mean square displacement (MSD) by

$$MSD (\Delta t) = \frac{1}{N} \sum_{i=1}^{N} \left\langle |\mathbf{r}_{i}(t + \Delta t) - \mathbf{r}_{i}(t)|^{2} \right\rangle_{t}$$
(7)

where N is the total number of diffusion ions; $r_i(t)$ is the displacement of the ith ion at time t; the bracket represents averaging over t. The diffusion coefficients for three-dimensional transport could be obtained by using the Einstein relation $D = \frac{\partial \text{MSD}}{\partial t}$. For the ion diffusion analysis, the initial 4 ps was removed to account for the equilibrium period, and only the last 6 ps data were analyzed.

The formation energies of H⁺ and Zn²⁺ intercalations into ZnVO were calculated based on the total energies of ZnVO and ions intercalated configurations. Herein, the electrolyte soaked ZnVO (Zn_{0.1}V₂O₅·2.5H₂O) was considered as the initial structure for the discharge process. Thus, the formation energies of H⁺ and Zn²⁺ intercalations into ZnVO, $E_{\rm fl}$ and $E_{\rm fl}$, respectively, are determined by the following equations

$$E_{f1} = \frac{E(H_x Z n_{0.1} V_2 O_5 \cdot 2.5 H_2 O) - E(Z n_{0.1} V_2 O_5 \cdot 2.5 H_2 O) - xE(H)}{x}$$
(8)

$$\frac{E(Zn_{0.1+x}V_2O_5 \cdot 2.5H_2O) - E(Zn_{0.1}V_2O_5 \cdot 2.5H_2O) - xE(Zn)}{x}$$

where E(H) is the energy of a single H atom, which is calculated from the relaxed H_2 structure; E(Zn) is the energy per Zn atom (hcp); $E(H_x Zn_{0.1} V_2 O_5 \cdot 2.5 H_2 O)$ and $E(Zn_{0.1+x} V_2 O_5 \cdot 2.5 H_2 O)$ are the total energies of H^+ and Zn^{2+} intercalated ZnVO, respectively.

The average formation energy of water intercalation into ZnVO can be calculated based on the total energy of dry ZnVO (Zn_{0.1}V₂O₅) and water intercalated ZnVO (Zn_{0.1}V₂O₅·xH₂O). The average formation energy of water intercalation, $E_{\rm f3}$, is calculated by

$$E_{f3} = \frac{E(Zn_{0.1}V_2O_5 \cdot xH_2O) - E(Zn_{0.1}V_2O_5) - xE(H_2O)}{x}$$
(10)

where $E(\mathrm{H_2O})$ is the total energy of a $\mathrm{H_2O}$ molecule in the gas phase. In addition, the average formation energy of solvent water, E_f4 , is calculated as

$$E_{\rm f4} = \frac{E(\text{solvent water}) - xE(H_2O)}{x}$$
 (11)

where E(solvent water) and x are the total energy of solvent water and number of waters, respectively. It should be noted that there are many different water arrangements in solvent water. Here, the models with solvent water in space groups of Cmc21, P63cm, and P1 are adopted to calculate the formation energy of solvent water.

ASSOCIATED CONTENT

Supporting Information

I

The Supporting Information is available free of charge at https://pubs.acs.org/doi/10.1021/acsnano.1c03684.

Additional XRD, SEM, TEM, HRTEM, SAED, TGA-DTA curves, nitrogen adsorption-desorption isotherms, and digital images of pristine ZnVO powders and ZnVO electrodes with immersion in different solutions. The cycle performance and rate performance of ZnVO electrodes. The kinetic behavior (CV, EIS, GITT), state-of-charge dependent composition, and phase changes of ZnVO cathode. The *in situ* XRD, *ex situ* XRD, XPS, SEM, STEM, Zn, V, and O mappings for ZnVO electrode at OCV, discharged and charged states. Structural and morphological characterization together with cycle performance of H-V₂O₅. Table of the electrochemical performance comparsion for the ZnVO nanobelts with some representative cathode materials in ZIBs (PDF)

AUTHOR INFORMATION

Corresponding Authors

Tao Wu – Department of Mechanical Engineering, University of South Carolina, Columbia, South Carolina 29201, United States; orcid.org/0000-0001-9543-0377;

Email: taowu@njust.edu.cn

Kevin Huang — Department of Mechanical Engineering, University of South Carolina, Columbia, South Carolina 29201, United States; orcid.org/0000-0002-1232-4593; Email: huang46@cec.sc.edu

Authors

Kaiyue Zhu – Department of Mechanical Engineering, University of South Carolina, Columbia, South Carolina 29201, United States

Wessel van den Bergh – Department of Biochemistry & Chemistry, University of South Carolina, Columbia, South Carolina 29201, United States

Morgan Stefik – Department of Biochemistry & Chemistry, University of South Carolina, Columbia, South Carolina 29201, United States

Complete contact information is available at: https://pubs.acs.org/10.1021/acsnano.1c03684

Notes

The authors declare no competing financial interest.

ACKNOWLEDGMENTS

K.Z., T.W., and K.H. thank the South Carolina Smart State Center program and National Science Foundation under award number CBET-1801284 for financial support. W.v.d.B. and M.S. acknowledge support by the National Science Foundation under award DMR-1752615. This work made use of the South Carolina SAXS Collaborative.

REFERENCES

- (1) Jia, X.; Liu, C.; Neale, Z. G.; Yang, J.; Cao, G. Active Materials for Aqueous Zinc Ion Batteries: Synthesis, Crystal Structure, Morphology, and Electrochemistry. *Chem. Rev.* **2020**, *120*, 7795–7866.
- (2) Zhang, N.; Chen, X.; Yu, M.; Niu, Z.; Cheng, F.; Chen, J. Materials Chemistry for Rechargeable Zinc-Ion Batteries. *Chem. Soc. Rev.* **2020**, 49, 4203–4219.
- (3) Tang, B.; Shan, L.; Liang, S.; Zhou, J. Issues and Opportunities Facing Aqueous Zinc-Ion Batteries. *Energy Environ. Sci.* **2019**, *12*, 3288–3304.
- (4) Song, M.; Tan, H.; Chao, D.; Fan, H. J. Recent Advances in Zn-Ion Batteries. Adv. Funct. Mater. 2018, 28, 1802564.

- (5) Ming, J.; Guo, J.; Xia, C.; Wang, W.; Alshareef, H. N. Zinc-Ion Batteries: Materials, Mechanisms, and Applications. *Mater. Sci. Eng., R* **2019**, *135*, 58–84.
- (6) Chao, D.; Zhou, W.; Xie, F.; Ye, C.; Li, H.; Jaroniec, M.; Qiao, S.-Z. Roadmap for Advanced Aqueous Batteries: From Design of Materials to Applications. *Sci. Adv.* **2020**, *6*, eaba4098.
- (7) Huang, J.; Guo, Z.; Ma, Y.; Bin, D.; Wang, Y.; Xia, Y. Recent Progress of Rechargeable Batteries Using Mild Aqueous Electrolytes. *Small Methods* **2019**, *3*, 1800272.
- (8) Wan, F.; Niu, Z. Design Strategies for Vanadium-based Aqueous Zinc-Ion Batteries. *Angew. Chem., Int. Ed.* **2019**, *58*, 16358–16367.
- (9) Blanc, L. E.; Kundu, D.; Nazar, L. F. Scientific Challenges for the Implementation of Zn-Ion Batteries. *Joule* **2020**, *4*, 771–799.
- (10) Zhu, K.; Wu, T.; Sun, S.; Wen, Y.; Huang, K. Electrode Materials for Practical Rechargeable Aqueous Zn-Ion Batteries: Challenges and Opportunities. *ChemElectroChem* **2020**, *7*, 2714–2724
- (11) Yan, M.; He, P.; Chen, Y.; Wang, S.; Wei, Q.; Zhao, K.; Xu, X.; An, Q.; Shuang, Y.; Shao, Y.; Mueller, K. T.; Mai, L.; Liu, J.; Yang, J. Water-Lubricated Intercalation in V_2O_5 ·n H_2O for High-Capacity and High-Rate Aqueous Rechargeable Zinc Batteries. *Adv. Mater.* **2018**, 30, 1703725.
- (12) Zhang, N.; Dong, Y.; Jia, M.; Bian, X.; Wang, Y.; Qiu, M.; Xu, J.; Liu, Y.; Jiao, L.; Cheng, F. Rechargeable Aqueous $\rm Zn-V_2O_5$ Battery with High Energy Density and Long Cycle Life. *ACS Energy Lett.* **2018**, 3, 1366–1372.
- (13) Pang, Q.; Sun, C.; Yu, Y.; Zhao, K.; Zhang, Z.; Voyles, P. M.; Chen, G.; Wei, Y.; Wang, X. $\rm H_2V_3O_8$ Nanowire/Graphene Electrodes for Aqueous Rechargeable Zinc Ion Batteries with High Rate Capability and Large Capacity. *Adv. Energy Mater.* **2018**, *8*, 1800144.
- (14) Zhu, K.; Wu, T.; Sun, S.; van den Bergh, W.; Stefik, M.; Huang, K. Synergistic H⁺/Zn²⁺ Dual Ion Insertion Mechanism in High-Capacity and Ultra-Stable Hydrated VO₂ Cathode for Aqueous Zn-Ion Batteries. *Energy Storage Mater.* **2020**, *29*, 60–70.
- (15) Li, C.; Zhang, X.; He, W.; Xu, G.; Sun, R. Cathode Materials For Rechargeable Zinc-Ion Batteries: From Synthesis to Mechanism and Applications. *J. Power Sources* **2020**, 449, 227596.
- (16) Zhu, Q.-N.; Wang, Z.-Y.; Wang, J.-W.; Liu, X.-Y.; Yang, D.; Cheng, L.-W.; Tang, M.-Y.; Qin, Y.; Wang, H. Challenges and Strategies for Ultrafast Aqueous Zinc-Ion Batteries. *Rare Met.* **2021**, 40, 309–328.
- (17) Hu, F.; Xie, D.; Zhao, D.; Song, G.; Zhu, K. Na₂V₆O₁₆·2.14H₂O Nanobelts as a Stable Cathode for Aqueous Zinc-Ion Batteries with Long-Term Cycling Performance. *J. Energy Chem.* **2019**, *38*, 185–191.
- (18) Cang, R.; Ye, K.; Zhu, K.; Yan, J.; Yin, J.; Cheng, K.; Wang, G.; Cao, D. Organic 3D Interconnected Graphene Aerogel as Cathode Materials for High-Performance Aqueous Zinc Ion Battery. *J. Energy Chem.* **2020**, *45*, 52–58.
- (19) Li, R.; Zhang, H.; Zheng, Q.; Li, X. Porous V_2O_5 Yolk-Shell Microspheres for Zinc Ion Battery Cathode: Activation Responsible for Enhanced Capacity and Rate Performance. *J. Mater. Chem. A* **2020**, *8*, 5186–5193.
- (20) Zhou, J.; Shan, L.; Wu, Z.; Guo, X.; Fang, G.; Liang, S. Investigation of V_2O_5 As a Low-Cost Rechargeable Aqueous Zinc Ion Battery Cathode. *Chem. Commun.* **2018**, *54*, 4457–4460.
- (21) Hu, P.; Zhu, T.; Ma, J.; Cai, C.; Hu, G.; Wang, X.; Liu, Z.; Zhou, L.; Mai, L. Porous V_2O_5 Microspheres: A High-Capacity Cathode Material for Aqueous Zinc-Ion Batteries. *Chem. Commun.* **2019**, 55, 8486–8489.
- (22) Greenwood, N. N.; Earnshaw, A. Chemistry of the Elements; Pergamon Press: Oxford, 1984; p 996.
- (23) Livage, J. Synthesis of Polyoxovanadates via "Chimie Douce". Coord. Chem. Rev. 1998, 178–180, 999–1018.
- (24) Hao, Y.; Zhang, S.; Tao, P.; Shen, T.; Huang, Z.; Yan, J.; Chen, Y. Pillaring Effect of K Ion Anchoring for Stable V_2O_5 -Based Zinc-Ion Battery Cathodes. *ChemNanoMat* **2020**, *6*, 797–805.
- (25) Zhang, S.; Tan, H.; Rui, X.; Yu, Y. Vanadium-Based Materials: Next Generation Electrodes Powering the Battery Revolution? *Acc. Chem. Res.* **2020**, *53*, 1660–1671.

- (26) He, P.; Zhang, G.; Liao, X.; Yan, M.; Xu, X.; An, Q.; Liu, J.; Mai, L. Sodium Ion Stabilized Vanadium Oxide Nanowire Cathode for High-Performance Zinc-Ion Batteries. *Adv. Energy Mater.* **2018**, *8*, 1702463.
- (27) Yang, Y.; Tang, Y.; Fang, G.; Shan, L.; Guo, J.; Zhang, W.; Wang, C.; Wang, L.; Zhou, J.; Liang, S. Li $^+$ Intercalated V₂O₅·nH₂O with Enlarged Layer Spacing and Fast Ion Diffusion as an Aqueous Zinc-Ion Battery Cathode. *Energy Environ. Sci.* **2018**, *11*, 3157–3162.
- (28) Liu, C.; Neale, Z.; Zheng, J.; Jia, X.; Huang, J.; Yan, M.; Tian, M.; Wang, M.; Yang, J.; Cao, G. Expanded Hydrated Vanadate for High-Performance Aqueous Zinc-Ion Batteries. *Energy Environ. Sci.* **2019**, *12*, 2273–2285.
- (29) Xia, C.; Guo, J.; Li, P.; Zhang, X.; Alshareef, H. N. Highly Stable Aqueous Zinc-Ion Storage Using a Layered Calcium Vanadium Oxide Bronze Cathode. *Angew. Chem., Int. Ed.* **2018**, *57*, 3943–3948.
- (30) Ming, F.; Liang, H.; Lei, Y.; Kandambeth, S.; Eddaoudi, M.; Alshareef, H. N. Layered $Mg_xV_2O_5$ ·n H_2O as Cathode Material for High Performance Aqueous Zinc Ion Batteries. *ACS Energy Lett.* **2018**, 3, 2602–2609.
- (31) Kundu, D.; Adams, B. D.; Duffort, V.; Vajargah, S. H.; Nazar, L. F. A High-Capacity and Long-Life Aqueous Rechargeable Zinc Battery Using a Metal Oxide Intercalation Cathode. *Nat. Energy* **2016**, *1*, 16119.
- (32) Zeng, X.; Hao, J.; Wang, Z.; Mao, J.; Guo, Z. Recent Progress and Perspectives on Aqueous Zn-Based Rechargeable Batteries with Mild Aqueous Electrolytes. *Energy Storage Mater.* **2019**, *20*, 410–437.
- (33) Parija, A.; Prendergast, D.; Banerjee, S. Evaluation of Multivalent Cation Insertion in Single- and Double-Layered Polymorphs of V₂O₅. ACS Appl. Mater. Interfaces **2017**, 9, 23756–23765.
- (34) Livage, J. Vanadium Pentoxide. Chem. Mater. 1991, 3, 578–593.
- (35) Wu, T.; Zhu, K.; Qin, C.; Huang, K. Unraveling the Role of Structural Water in Bilayer V_2O_5 during Zn^{2+} -Intercalation: Insights from DFT Calculations. *J. Mater. Chem. A* **2019**, 7, 5612–5620.
- (36) Zhu, K.; Wu, T.; Huang, K. A High Capacity Bilayer Cathode for Aqueous Zn-Ion Batteries. ACS Nano 2019, 13, 14447–14458.
- (37) Xing, Z.; Wang, S.; Yu, A.; Chen, Z. Aqueous Intercalation-Type Electrode Materials for Grid-Level Energy Storage: Beyond the Limits of Lithium and Sodium. *Nano Energy* **2018**, *50*, 229–244.
- (38) Wang, L.; Huang, K.-W.; Chen, J.; Zheng, J. Ultralong Cycle Stability of Aqueous Zinc-Ion Batteries with Zinc Vanadium Oxide Cathodes. *Sci. Adv.* **2019**, *5*, eaax4279.
- (39) He, P.; Chen, Q.; Yan, M.; Xu, X.; Zhou, L.; Mai, L.; Nan, C.-W. Building Better Zinc-Ion Batteries: A Materials Perspective. *EnergyChem.* **2019**, *1*, 100022.
- (40) Wang, X.; Li, Y.; Wang, S.; Zhou, F.; Das, P.; Sun, C.; Zheng, S.; Wu, Z.-S. 2D Amorphous V₂O₅/Graphene Heterostructures for High-Safety Aqueous Zn-Ion Batteries with Unprecedented Capacity and Ultrahigh Rate Capability. *Adv. Energy Mater.* **2020**, *10*, 2000081.
- (41) Liu, S.; Zhu, H.; Zhang, B.; Li, G.; Zhu, H.; Ren, Y.; Geng, H.; Yang, Y.; Liu, Q.; Li, C. C. Tuning the Kinetics of Zinc-Ion Insertion/Extraction in V_2O_5 by *in Situ* Polyaniline Intercalation Enables Improved Aqueous Zinc-Ion Storage Performance. *Adv. Mater.* **2020**, 32, 2001113.
- (42) Zhu, K.; Wu, T.; Huang, K. $NaCa_{0.6}V_6O_{16}\cdot 3H_2O$ as an Ultra-Stable Cathode for Zn-Ion Batteries: The Roles of Pre-Inserted Dual-Cations and Structural Water in V_3O_8 Layer. *Adv. Energy Mater.* **2019**, 9, 1901968.
- (43) Zhang, L.; Chen, L.; Zhou, X.; Liu, Z. Towards High-Voltage Aqueous Metal-Ion Batteries beyond 1.5 V: The Zinc/Zinc Hexacyanoferrate System. *Adv. Energy Mater.* **2015**, *5*, 1400930.
- (44) Zhang, N.; Cheng, F.; Liu, J.; Wang, L.; Long, X.; Liu, X.; Li, F.; Chen, J. Rechargeable Aqueous Zinc-Manganese Dioxide Batteries with High Energy and Power Densities. *Nat. Commun.* **2017**, *8*, 405.
- (45) Xia, C.; Guo, J.; Lei, Y.; Liang, H.; Zhao, C.; Alshareef, H. N. Rechargeable Aqueous Zinc-Ion Battery Based on Porous Framework Zinc Pyrovanadate Intercalation Cathode. *Adv. Mater.* **2018**, *30*, 1705580.

- (46) Soundharrajan, V.; Sambandam, B.; Kim, S.; Alfaruqi, M. H.; Putro, D. Y.; Jo, J.; Kim, S.; Mathew, V.; Sun, Y.-K.; Kim, J. Na₂V₆O₁₆· 3H₂O Barnesite Nanorod: An Open Door to Display a Stable and High Energy for Aqueous Rechargeable Zn-Ion Batteries as Cathodes. *Nano Lett.* **2018**, *18*, 2402–2410.
- (47) Sambandam, B.; Soundharrajan, V.; Kim, S.; Alfaruqi, M. H.; Jo, J.; Kim, S.; Mathew, V.; Sun, Y.-k.; Kim, J. $K_2V_6O_{16}$ -2.7H $_2O$ Nanorod Cathode: An Advanced Intercalation System for High Energy Aqueous Rechargeable Zn-Ion Batteries. *J. Mater. Chem. A* **2018**, *6*, 15530–15539.
- (48) He, P.; Yan, M.; Zhang, G.; Sun, R.; Chen, L.; An, Q.; Mai, L. Layered VS₂ Nanosheet-Based Aqueous Zn Ion Battery Cathode. *Adv. Energy Mater.* **2017**, *7*, 1601920.
- (49) Zhao, Q.; Huang, W.; Luo, Z.; Liu, L.; Lu, Y.; Li, Y.; Li, L.; Hu, J.; Ma, H.; Chen, J. High-Capacity Aqueous Zinc Batteries Using Sustainable Quinone Electrodes. *Sci. Adv.* **2018**, *4*, eaao1761.
- (50) Zhang, Y.; Chen, Z.; Qiu, H.; Yang, W.; Zhao, Z.; Zhao, J.; Cui, G. Pursuit of Reversible Zn Electrochemistry: A Time-Honored Challenge towards Low-Cost and Green Energy Storage. NPG Asia Mater. 2020, 12, 4.
- (51) Wan, F.; Zhang, L.; Dai, X.; Wang, X.; Niu, Z.; Chen, J. Aqueous Rechargeable Zinc/Sodium Vanadate Batteries with Enhanced Performance from Simultaneous Insertion of Dual Carriers. *Nat. Commun.* **2018**, *9*, 1656.
- (52) Zhang, N.; Jia, M.; Dong, Y.; Wang, Y.; Xu, J.; Liu, Y.; Jiao, L.; Cheng, F. Hydrated Layered Vanadium Oxide as a Highly Reversible Cathode for Rechargeable Aqueous Zinc Batteries. *Adv. Funct. Mater.* **2019**, *29*, 1807331.
- (53) Li, C.; Yuan, W.; Li, C.; Wang, H.; Wang, L.; Liu, Y.; Zhang, N. Boosting $\text{Li}_3\text{V}_2(\text{PO}_4)_3$ Cathode Stability Using a Concentrated Aqueous Electrolyte for High-Voltage Zinc Batteries. *Chem. Commun.* **2021**, *57*, 4319–4322.
- (54) Guo, X.; Fang, G.; Zhang, W.; Zhou, J.; Shan, L.; Wang, L.; Wang, C.; Lin, T.; Tang, Y.; Liang, S. Mechanistic Insights of Zn²⁺ Storage in Sodium Vanadates. *Adv. Energy Mater.* **2018**, *8*, 1801819.
- (55) Kresse, G.; Hafner, J. Ab Initio Molecular-Dynamics Simulation of the Liquid-Metal-Amorphous-Semiconductor Transition in Germanium. Phys. Rev. B: Condens. Matter Mater. Phys. 1994, 49, 14251–14260
- (56) Kresse, G.; Hafner, J. Ab Initio Molecular Dynamics for Liquid Metals. Phys. Rev. B: Condens. Matter Mater. Phys. 1993, 47, 558-561.
- (57) Perdew, J. P.; Burke, K.; Ernzerhof, M. Generalized Gradient Approximation Made Simple. *Phys. Rev. Lett.* **1996**, 77, 3865–3868.
- (58) Blöchl, P. E. Projector Augmented-Wave Method. Phys. Rev. B: Condens. Matter Mater. Phys. 1994, 50, 17953–17979.
- (59) Kresse, G.; Joubert, D. From Ultrasoft Pseudopotentials to the Projector Augmented-Wave Method. *Phys. Rev. B: Condens. Matter Mater. Phys.* **1999**, *59*, 1758–1775.
- (60) Anisimov, V. I.; Aryasetiawan, F.; Lichtenstein, A. I. First-Principles Calculations of the Electronic Structure and Spectra of Strongly Correlated Systems: The LDA + U Method. *J. Phys.: Condens. Matter* **1997**, *9*, 767–808.
- (61) Grimme, S.; Ehrlich, S.; Goerigk, L. Effect of the Damping Function in Dispersion Corrected Density Functional Theory. *J. Comput. Chem.* **2011**, 32, 1456–1465.
- (62) Nose, S. Constant Temperature Molecular Dynamics Methods. *Prog. Theor. Phys. Suppl.* **1991**, *103*, 1–46.
- (63) Nosé, S. A Unified Formulation of he Constant Temperature Molecular Dynamics Methods. *J. Chem. Phys.* **1984**, *81*, 511–519.
- (64) Bylander, D.; Kleinman, L. Energy Fluctuations Induced by the Nosé Thermostat. *Phys. Rev. B: Condens. Matter Mater. Phys.* **1992**, 46, 13756.